



Research Article

Investigation of thermomagnetic gravitational convection and energy distribution in a vertical layer of ferrofluid

Md. Habibur RAHMAN¹

¹Department of Mathematics, Khulna University of Engineering & Technology, Khulna, 9203, Bangladesh

ARTICLE INFO

Article history

Received: 10 June 2023

Revised: 11 October 2023

Accepted: 11 October 2023

Keywords:

Convection; Energy; Ferrofluid;
Instability; Magnetic Field

ABSTRACT

The applied magnetic field and its inclination angle play important roles in flow stabilization and energy distribution in the flow domain. In this article, the linear stability characteristics and energy distribution due to the combined influence of thermal, magnetic, and gravitational forces in a vertical layer of ferrofluid enclosed by two differentially heated walls are investigated. The objective of this article is to investigate the combined effects of thermogravitational buoyancy and magnetic forces and provide parametric guidance for mixed magnetogravitational thermal experiments. The numerical results are obtained by the pseudo-spectral Chebyshev expansion method. It is found that the qualitative change in the shape of the instability boundaries and the area of flow stability expands significantly when the field inclination angle increases. The destabilizing magnetic field variation effect is most pronounced in the near-wall regions, especially near the cold wall. However, the viscous dissipation near the cold wall is also stronger than that close to the hot wall. Consequently, the overall instability pattern shifts toward the hot wall. The thermomagnetic perturbations arising in the layer of ferrofluid tend to make the magnetic and magnetization fields more uniform near the walls. The instability is mostly driven by gravitational buoyancy due to thermal effects compared to magnetic effects. The perturbed kinetic energy is lost due to viscous dissipation and modification of the applied magnetic field in the flow domain. Ferrofluids under the effects of thermal, magnetic, and gravitational forces have potential applications in cancer detection, MRI scanning, oil separation from water, tunable optical filters, digital data storage, vibration dampening, energy conversion devices, etc., and many other engineering branches.

Cite this article as: Rahman MH. Investigation of thermomagnetic gravitational convection and energy distribution in a vertical layer of ferrofluid. J Ther Eng 2024;10(4):936–953.

INTRODUCTION

Ferrofluid is a unique liquid that exhibits magnetic properties. It is composed of tiny magnetic particles, typically magnetite (Fe_3O_4) or hematite (Fe_2O_3), suspended in

a carrier fluid, such as a hydrocarbon or a water-based solution. The magnetic particles are usually coated with a surfactant to prevent them from clumping together. Ferrofluid was initially developed for technical applications, such as in

***Corresponding author.**

*E-mail address: hrahman180@gmail.com, hrahman180@math.kuet.ac.bd

This paper was recommended for publication in revised form by Editor-in-Chief Ahmet Selim Dalkılıç



mechanical seals to maintain lubrication and reduce friction in rotating machinery and controlling heat transfer. However, they have also become popular in various artistic and novelty applications due to their mesmerizing properties. Ferrofluid was first promoted by NASA in the 1960s as a way to manage fuel in space. Since then, it has found various applications in engineering, electronics, and art due to its intriguing properties. While a magnetic field present, ferrofluid aligns itself parallel to the lines of the magnetic field, developing fascinating spikes, patterns, and shapes. It also exhibits fluid behavior, allowing it to flow and respond to external forces. In the field of medicine, researchers have explored the use of ferrofluids for targeted drug delivery and imaging applications. It's worth noting that handling ferrofluid requires some precautions as it can stain surfaces and be challenging to clean. Additionally, direct contact with skin should be avoided, as the surfactant in the fluid can cause skin irritation. The temperature at which a material undergoes a phase transition and loses its ferromagnetic properties named the Curie point according to the name of French physicist Pierre Curie. The Curie point, also known as the Curie temperature, is a fundamental concept in the field of magnetism. Below the Curie point, materials can exhibit spontaneous magnetization, meaning they can become permanently magnetized while external magnetic field present. However, as temperature increases and approaches to the Curie point, material's magnetization decreases, and eventually, it becomes non-magnetic. An exact Curie point temperature varies depending on material. Different substances have different atomic structures and magnetic properties, so their Curie points can differ significantly. For example, iron, a common ferromagnetic material, has the Curie point of around 770 degrees Celsius, while nickel has the Curie point of approximately 355 degrees Celsius. Above the Curie point, material transitions into a paramagnetic or diamagnetic state, depending on its specific characteristics. In these states, material does not exhibit permanent magnetization and instead weakly responds to magnetic fields.

Artificial ferrofluid, also known as synthetic ferrofluid, refers to a type of ferrofluid that is artificially created in a laboratory setting rather than being naturally occurring. Synthetic ferrofluids are engineered to possess specific properties and characteristics for various applications. To create artificial ferrofluid, researchers typically start with a carrier fluid, such as a hydrocarbon or water-based solution, and add magnetic nanoparticles to it. These nanoparticles are usually composed of materials like iron oxide (such as magnetite) or iron-platinum alloys. Nanoparticles are carefully dispersed within a carrier fluid, and surfactant is added to prevent agglomeration and maintain stability. The composition and magnetic nanoparticle size, as well as the choice of carrier fluid and surfactant can be adjusted to customize the properties of artificial ferrofluid. This allows researchers to control factors such as viscosity, magnetic response, stability, and other characteristics

based on the intended application. The applications of artificial ferrofluids span across diverse fields. They are used in technologies such as mechanical engineering, electronics, acoustics, and medicine. For example, in speakers and headphones, synthetic ferrofluids are utilized to dampen unwanted vibrations and improve sound quality. Ongoing research and development continue to expand the potential uses and optimize the performance of artificial ferrofluids in various fields. When a ferrofluid experiences temperature variations, the resulting density variations induce a magnetic buoyancy force. This force leads to fluid motion known as gravitational convection, where warmer fluid rises and cooler fluid sinks. Gravitational convection is a natural convection process driven by buoyancy and plays a significant role in redistributing heat within ferrofluids and other systems. While the investigation of flows in states where gravitational buoyancy-driven convection is not possible may deviate from traditional studies, it opens up avenues for prototype applications [1, 2]. The Rayleigh number tends to approach zero in outer space and microelectronic devices, where gravitational forces are negligible. Exploring non-gravitational flow phenomena is important for microscale systems, space exploration, and various applications where understanding fluid behavior in the absence of gravitational convection. Magnetoconvection, governed by the magnetic Rayleigh number, offers a unique advantage over buoyancy-driven convection. It can be induced in gravity-free environments and is particularly useful in congested spaces of microelectronic devices. The utilization of magneto-convective flows enables efficient heat removal, making it a promising approach for enhancing thermal management in microscale applications [3, 4]. The complex composition of ferrofluids necessitates extensive experimental investigations into their flows [5]. However, conducting experiments directly in the working conditions of ferrofluids, whether within microelectronic devices or in space, poses significant challenges. As a result, experimental studies often rely on ground-based experiments within finite-size containers as a practical alternative. These experiments provide valuable insights into the behavior of ferrofluid flows despite the limitations imposed by the experimental setup [6, 7]. Thus, the influence of gravitational convection on the flows of non-isothermal ferrofluid cannot be avoided. Thermogravitational convection mechanism is a direct result of the buoyancy force that arises from fluids thermal expansion kept in non-uniform heating [8, 9]. It is an example of a thermally induced hydrodynamic instability [10].

The goal of this article is to analyze and investigate the instabilities that arise due to the interactivity of gravitational buoyancy forces and magnetic Kelvin forces. The focus is on understanding the intricate dynamics and behaviors resulting from the interplay of these two forces. The aim of this research is to provide parametric guidance for mixed magneto-gravitational thermal experiments. One key aspect that sets the present research apart from previous

studies [2, 11-16] focusing on the combined effects arising from the interactivity of gravitational buoyancy force and magnetic Kelvin force. The effect of the magnetic field on the natural convective flow for a typical ferrofluid, magnetite (Fe_3O_4) over a vertical radiate plate using streamwise sinusoidal variation in surface temperature are investigated by El-Zahar et al. [17]. The applied magnetic field to the ferrofluid originates a dragging force that reduces the ferrofluid velocity, while the temperature curves are boosted. This type of investigation can be beneficial in manufacturing processes, heat resources, and development of energy transportation. By applying the finite volume method, a mixed convective flow of kerosene-cobalt ferrofluid in a lid-driven square cavity under partial slip condition is analyzed numerically by Chamkha et al. [18]. They used an enclosure with two vertical walls heated partially with a constant temperature keeping the horizontal moving walls in adiabatic. It is found that the augmentation of the ferro-magnetic particles volume fraction affects the heat transfer rate under the effects of magnetic field and the movement of opposite directional horizontal walls. The effect of magnetic field reduces heat transfer rate due to the dissipation of the boundary layer gradient. In contrast, the heat transfer rate progressed due to the movement of the opposite directional horizontal walls. Taskesen et al. [19] investigated the experimental results utilizing mono (Fe_3O_4 and Cu) and hybrid (Fe_3O_4-Cu) type water-based nanofluid with very small nanoparticle volume concentrations under laminar flow conditions, and compared to the results obtained by ANN (Artificial Neural Network). These findings demonstrate that a suitable way is developed by the use of ANN to predict the performance of convective heat transfer rate of hybrid nanofluid in a magnetic field effect. The numerical results of this study for a set of particular values of governing parameters for threshold of gravitational convection agree closely with those results for same parameter values are obtained by Belyaev and Smorodin [20]. However, for onset of the magnetic convection, the numerical results also exhibit good agreement with the similar results reported in Finlayson [11]. To enable a direct comparison the same specific parameter values prompted by the recent studies reported in literature to date [16, 21-23] are considered and flow instabilities for wider parametric ranges also to be investigated to provide the proper instructions for future experiments. The physical characteristics of instabilities are reported under normal magnetic field effect in [15] and inclined magnetic field effect in [23], but it is not clear adequately what the dominant physical mechanism is when both magnetic effect and thermal effect are non-zero.

The novelty of this article is to provide proper answer about the dominant roles of various physical mechanisms at what exact values of the governing parameters and other remaining questions. In order to competent answer these the perturbation kinetic energy balance equations to be used and the corresponding energy balance results for

linearized disturbances to be investigated in detail in this article.

GOVERNING EQUATIONS OF THE PROBLEM

An experimental configuration is considered where a layer of ferrofluid is placed between two vertically oriented plates, as illustrated in Figure 1. The right-handed Cartesian coordinates (x, y, z) are utilized to describe the system, the origin positioned at middle between two plates. The non-magnetic plates extend infinitely in the vertical direction, and their positions are defined as $x = \pm d$. Additionally, there is a gravitational field represented by the vector \vec{g} , which has components $(0, -g, 0)$ pointing downwards. Temperature of the left plate is denoted as $T_* - \Theta$, while temperature of the right plate is represented as $T_* + \Theta$. The system is maintained in a uniform outer magnetic field.

The field has intensity \vec{H}^e and it is inclined at certain angles, related to the plates. The δ is defined as an inclination angle related to the x axis. Consequently, the applied field's x -component is provided by the formula $H_x^e = H^e \cos \delta$, while the component parallel to the walls is $H^e \sin \delta$. To further describe the magnetic field orientation, the γ introduced as an angle made by the projection of applied field on the yz plane with the positive y axis. This allows us to express the y -component of applied field as $H_y^e = H^e \sin \delta \cos \gamma$, as well as the z -component as $H_z^e = H^e \sin \delta \sin \gamma$. An induced magnetic field inside

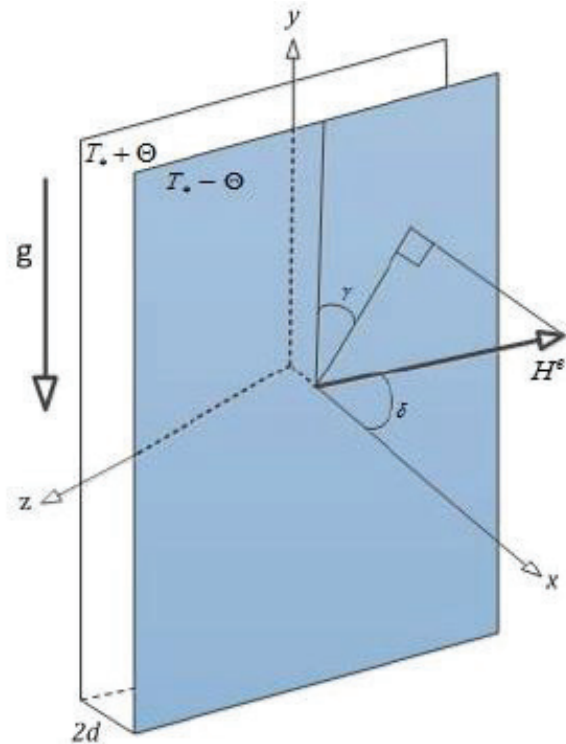


Figure 1. Schematic view of the problem geometry.

fluids layer is developed by applied outer magnetic field, denoted as \vec{H} , with a magnitude of H . This induced magnetic field \vec{H} , leads to fluid magnetization, represented by \vec{M} , with a magnitude of M . In this formulation, we assume that the magnetization vector is aligned with the inside magnetic field, resulting in $\vec{M} = \chi_* \vec{H}$ where χ_* represents the fluid’s integral magnetic susceptibility. This assumption allows us to establish a direct relationship between magnetic field and fluids magnetization. The susceptibility χ_* quantifies the fluid’s reaction to the applied field. It characterizes how easily the fluid can become magnetized in the presence of magnetic field. A higher value of χ_* indicates a stronger magnetic response, while a lower value indicates a weaker response. Assuming a small temperature variance of 2θ between two plates, we employ the Boussinesq approximation to simplify the governing equations. The Boussinesq approximation is applied to the equations of continuity, Navier-Stokes, as well as thermal energy. Additionally, we consider the Maxwell equations in the magneto-static form, since ferrofluids typically have negligible electrical conductivity [24]. Following the discussion in Suslov et al. [25], the governing equations for velocity, $\vec{v} = (u, v, w)$, pressure p , magnetization in \vec{M} , magnetic field \vec{H} , and temperature T , can be expressed as follows:

$$\nabla \cdot \vec{v} = 0, \tag{1}$$

$$\rho_* \frac{\partial \vec{v}}{\partial t} + \rho_* \vec{v} \cdot \nabla \vec{v} = -\nabla p + \rho_* \vec{g} + \eta_* \nabla^2 \vec{v} + \mu_0 \vec{M} \nabla \vec{H}, \tag{2}$$

$$\frac{\partial T}{\partial t} + \vec{v} \cdot \nabla T = \kappa_* \nabla^2 T, \tag{3}$$

$$\nabla \times \vec{H} = \vec{0}, \quad \nabla \cdot \vec{B} = 0, \tag{4}$$

by introducing

$$\vec{B} = \mu_0(\vec{H} + \vec{M}) \quad \text{and} \quad \vec{M} = \frac{(H, T)M}{H} \vec{H}, \tag{5}$$

where t represents time, T denotes temperature, p stands for pressure, \vec{B} represents magnetic flux density, ρ_* signifies density, η_* represents dynamic viscosity, and κ_* represents thermal diffusivity. The magnetic constant is denoted as μ_0 . The subscript $*$ typically represents the fluids properties assessed at a specific temperature T_* as well as a particular magnetic field \vec{H}_* . It is used to distinguish these reference values from their variable counterparts in the governing equations. The boundary conditions for velocity and temperature are defined as:

$$\vec{v} = \vec{0}, \quad \text{and} \quad \nabla T = \pm \theta \quad \text{at} \quad x = \mp d. \tag{6}$$

The boundary conditions for magnetic field are defined as follows:

$$\vec{\eta} \times (\vec{H}^e - \vec{H}) = \vec{0}, \quad \text{and} \quad \vec{\eta} \cdot (\vec{B}^e - \vec{B}) = 0 \quad \text{at} \quad x = \pm d, \tag{7}$$

where, superscript ‘e’ signifies the external field to the fluid’s layer and $\vec{\eta} = (1, 0, 0)$ is the perpendicular unit vector to the plates. A non-zero gravity is an important factor in the governing equations and the features of combined thermomagnetic-gravitational convection to be discussed in detail below. The gravity vector \vec{g} is defined with constant components $(0, -g, 0)$, acting opposite to the positive y -axis and parallel to the plates. To maintain consistency for the Boussinesq approximation, which is valid for minor temperature variance between two plates, the variation of fluid density along with temperature T is only addressed in the buoyancy component of the equation (2). The density variation is expressed as:

$$\rho = [1 - (T - T_*)\beta_*]\rho_*, \tag{8}$$

where β_* represents the thermal expansion coefficient.

Nondimensionalisation of Equations and Parameters

The equations governing the phenomenon as well as their boundary conditions are nondimensionalized with length, temperature, velocity, as well as thermodynamic pressure as reference quantities

$$(x, y, z) = (x', y', z')d, \quad \vec{v} = \frac{\eta_*}{\rho_* d} \vec{v}',$$

$$P = \frac{\eta_*^2}{\rho_* d^2} P', \quad t = \frac{\rho_* d^2}{\eta_*} t',$$

$$\vec{g} = g \vec{e}_g, \quad \vec{H} = \frac{\kappa \theta}{1 + \chi} \vec{H}', \quad \Delta T = \theta \theta', \quad \vec{M} = \frac{\kappa \theta}{1 + \chi} \vec{M}'$$

where η_* represents the dynamic viscosity and ρ_* represents the density at T_* . The vector $\vec{e}_g = (0, -1, 0)$ denotes a unit vector in the direction of the y -axis. Additionally, the quantity d represents half of the distance between two vertical plates. Finally, after eliminating all primes for avoiding the complexity, we have

$$\nabla \cdot \vec{v} = 0, \tag{9}$$

$$\frac{\partial \vec{v}}{\partial t} + \vec{v} \cdot \nabla \vec{v} + \nabla P = \nabla^2 \vec{v} - Gr \theta \vec{e}_g - Gr_m \theta \nabla H, \tag{10}$$

$$\frac{\partial \theta}{\partial t} + \vec{v} \cdot \nabla \theta - \frac{1}{Pr} \nabla^2 \theta = 0, \quad (11)$$

$$\nabla \times \vec{H} = \vec{0}, \quad (12)$$

$$\nabla \cdot \vec{H}(1 + \chi_*) + \nabla H \cdot \vec{e}_* (\chi - \chi_*) - \nabla \theta \cdot \vec{e}_* (1 + \chi) = 0, \quad (13)$$

$$\vec{M} = \vec{e}_* [(H - N)(\chi - \chi_*) - \theta(1 + \chi)] + \chi_* \vec{H}, \quad (14)$$

using boundary conditions as follows:

$$[\vec{H}^e - \{(H - N)(\chi - \chi_*) \mp \vec{e}_* (1 + \chi)\} - \vec{H}(1 + \chi_*)] \cdot \vec{n} = 0, \quad (15)$$

$$\vec{v} = \vec{0} \text{ and } \theta = \mp 1 \text{ at } x = \pm 1. \quad (16)$$

The parameters in this problem that do not have any dimensions are presented as follows:

$$Pr = \frac{\eta_*}{\rho_* K_*}, Gr_m = \frac{\rho_* \mu_0 K^2 \theta^2 d^2}{\eta_*^2 (1 + \chi)}, Gr = \frac{\rho_*^2 \beta_* \theta g d^3}{\eta_*^2}, N = \frac{(1 + \chi) H_*}{K \Theta}. \quad (17)$$

The magnetic Grashof number, Gr_m has a relation to the magnetic Rayleigh number, Ra_m and defined as $Ra_m = Pr Gr_m$. Thermal Grashof number, denoted by Gr and magnetic Grashof number, denoted by Gr_m are dimensionless parameters that characterize the relative importance of buoyancy and magnetic forces in a fluid system. The Grashof number quantify the ratio of the magnitudes of these forces to viscous forces. On the other hand, the Prandtl number, denoted by Pr , is a dimensionless quantity that represents the ratio of kinematic viscosity to thermal diffusivity in a fluid which can be used in calculation of heat transfer, and also free and forced convection depending on the fluid properties together, these parameters play a crucial role in understanding the behavior of fluid systems. The values of Gr , Gr_m , and Pr act as the dominant factors of buoyancy, magnetic, and thermal effects, respectively, in a given fluid flow or a heat transfer scenario. The parameter N serves as a measurement of the magnetic field strength at reference point, relative to the change in fluid magnetization caused by the thermal effects. It provides a quantifiable indication of the ratio between the magnetic field's influence and the thermal impacts on the fluid magnetization. The standard parameter values are used for the recent experiments [16, 21]. Based on such physical quantities the estimated value of Prandtl number, by Pr is approximately 55, and it is used in computations for this article.

Linearized Perturbation Equations with Basic State

To explore the linear stability of the basic state, we consider a typical normal form representation of the perturbed variables. This representation assumes that the disturbances

are infinitesimal and periodic in the directions of the coordinate axes of y and z . The perturbation quantities can be expressed as

$$(\vec{v}, P, \theta, \vec{M}, \vec{H}, H) = (\vec{v}_0, P_0, \theta_0, \vec{M}_0, \vec{H}_0, H_0) + [(\vec{v}_1(x), P_1(x), \theta_1(x), \vec{M}_1(x), \vec{H}_1(x), H_1(x)) \times e^{\sigma t + i(\alpha y + \beta z)} + c.c.] \quad (18)$$

where “c.c.” stands for the complex conjugate of the formula in brackets, α and β are valid wavenumbers in the directions of the y - and z axes, respectively, and “ σ ” is the complex amplifying rate. The σ is decomposed into real (σ^R) and imaginary (σ^I) components, representing the growth rate and oscillatory behavior, respectively. In order to accomplish the equation (12) identically, it is useful to add the magnetic potential perturbation $\phi_1(x)e^{\sigma t + i(\alpha y + \beta z)}$ to ensure that $\vec{H}_1(x) = [D\phi_1, i\alpha\phi_1, i\beta\phi_1]^T$ and using Squire's transforms:

$$\left. \begin{aligned} (x, y, z) &= (\tilde{x}, \tilde{y}, \tilde{z}), \theta_0 = \tilde{\theta}_0, H_{x0} = \tilde{H}_{x0}, H_0 = \tilde{H}_0, \alpha^2 + \beta^2 = \tilde{\alpha}^2, \\ \beta &= \tilde{\beta}, \sigma = \tilde{\sigma}, \alpha v_1 + \beta w_1 = \tilde{\alpha} \tilde{v}, u_1 = \tilde{u}, w_1 = \tilde{w}, P_1 = \tilde{P}, \theta_1 = \tilde{\theta}, \\ \phi_1 &= \tilde{\phi}, Pr = \tilde{Pr}, Gr_m = \tilde{Gr}_m, \alpha Gr = \tilde{\alpha} \tilde{Gr}, \chi_* = \tilde{\chi}_*, \chi = \tilde{\chi}, \\ e_{10*} &= \tilde{e}_{10*}, e_{10} = \tilde{e}_{10}, \alpha e_{20} + \beta e_{30} = \tilde{\alpha} \tilde{e}_{20}, \alpha e_{20*} + \beta e_{30*} = \tilde{\alpha} \tilde{e}_{20*}. \end{aligned} \right\} \quad (19)$$

It is possible to formulate the linearized perturbed equations as follows:

$$D\tilde{u} + i\tilde{\alpha}\tilde{v} = 0, \quad (20)$$

$$\begin{aligned} \tilde{\sigma}\tilde{u} + (\tilde{\alpha}^2 + i\tilde{\alpha}\tilde{v}_0 - D^2)\tilde{u} + D\tilde{P} + \tilde{e}_{10}\tilde{Gr}_m D\tilde{H}_{x0}\tilde{\theta} \\ + \tilde{Gr}_m\tilde{\theta}_0\tilde{e}_{10}D^2\tilde{\phi} + \tilde{Gr}_m\tilde{\theta}_0 \left[i\tilde{\alpha}\tilde{e}_{20} + (1 - \tilde{e}_{10}^2)\frac{D\tilde{H}_{x0}}{\tilde{H}_0} \right] D\tilde{\phi} \\ - i\tilde{\alpha}\tilde{Gr}_m\tilde{\theta}_0\tilde{e}_{10}\tilde{e}_{20}\frac{D\tilde{H}_{x0}}{\tilde{H}_0}\tilde{\phi} = 0, \end{aligned} \quad (21)$$

$$\begin{aligned} \tilde{\sigma}\tilde{v} + D\tilde{v}_0\tilde{u} + (\tilde{\alpha}^2 + i\tilde{\alpha}\tilde{v}_0 - D^2)\tilde{v} + i\tilde{\alpha}\tilde{P} \\ - \tilde{Gr}\tilde{\theta} + \tilde{\alpha}\tilde{Gr}_m\tilde{\theta}_0(i\tilde{e}_{10}D\tilde{\phi} - \tilde{\alpha}\tilde{e}_{20}\tilde{\phi}) = 0, \end{aligned} \quad (22)$$

$$\begin{aligned} \tilde{\sigma}\tilde{w} + (\tilde{\alpha}^2 + i\tilde{\alpha}\tilde{v}_0 - D^2)\tilde{w} + i\tilde{\beta}\tilde{P} \\ + \tilde{\beta}\tilde{Gr}_m\tilde{\theta}_0(i\tilde{e}_{10}D\tilde{\phi} - \tilde{\alpha}\tilde{e}_{20}\tilde{\phi}) = 0, \end{aligned} \quad (23)$$

$$\tilde{\sigma}\tilde{\theta} + D\tilde{\theta}_0\tilde{u} + \left(\frac{\tilde{\alpha}^2 - D^2}{\tilde{Pr}} + i\tilde{\alpha}\tilde{v}_0 \right) \tilde{\theta} = 0, \quad (24)$$

$$\begin{aligned} (D^2 - \tilde{\alpha}^2)\tilde{\phi} - \frac{\tilde{\chi} - \tilde{\chi}_*}{1 + \tilde{\chi}_*} \tilde{\alpha}\tilde{e}_{20} \left[\tilde{\alpha}\tilde{e}_{20*} + i\tilde{e}_{10*}\tilde{e}_{10}\frac{D\tilde{H}_{x0}}{\tilde{H}_0} \right] \tilde{\phi} + \\ \frac{\tilde{\chi} - \tilde{\chi}_*}{1 + \tilde{\chi}_*} \left[i\tilde{\alpha}(\tilde{e}_{10}\tilde{e}_{20*} + \tilde{e}_{10*}\tilde{e}_{20}) \right. \\ \left. + \tilde{e}_{10*}(1 - \tilde{e}_{10}^2)\frac{D\tilde{H}_{x0}}{\tilde{H}_0} \right] D\phi + \frac{\tilde{\chi} - \tilde{\chi}_*}{1 + \tilde{\chi}_*} \tilde{e}_{10*}\tilde{e}_{10}D^2\tilde{\phi} \\ - \frac{1 + \tilde{\chi}}{1 + \tilde{\chi}_*} [i\tilde{\alpha}\tilde{e}_{20*} + \tilde{e}_{10*}D]\tilde{\theta} = 0, \end{aligned} \quad (25)$$

with their boundary conditions are

$$(1 + \tilde{\chi}_*)D\tilde{\phi} \pm [\tilde{\alpha}|\tilde{\phi} + \tilde{e}_{10*}(\tilde{\chi} - \tilde{\chi}_*) (i\tilde{\alpha}\tilde{e}_{20} + \tilde{e}_{10}D)\tilde{\phi}] = 0, \quad (26)$$

$$\tilde{u} = \tilde{v} = \tilde{\omega} = \theta = 0 \text{ at } \tilde{x} = \pm 1. \quad (27)$$

By setting $\beta = w = 0$, we can simplify the remaining equations (20)–(27) and obtain an equivalent two-dimensional problem. This reduction in dimensionality allows us for a significant reduction in computational cost when performing stability calculations.

Methodology

The resulting linearized equations (20)–(25) with boundary conditions (26) and (27) are discretized and the numerical results are obtained by utilizing the pseudo-spectral Chebyshev expansion methods, which are reported in [26, 27] and implemented in [22, 28]. The numerical results of this problem are obtained by solving the corresponding equations with the help of MATLAB software.

RESULTS AND DISCUSSION

Comparison of Numerical Results

To facilitate a comparison with previous findings, we calculated the critical values of the controlling parameters that govern the convection to begin. Specifically, we consider a perpendicular orientation of the outer magnetic field with intensity $H^e = 100$. The critical values for the

threshold of gravitational convection are determined for a Prandtl number $Pr = 7$, and a particular wave number denoted by $\tilde{\alpha}$. The set of critical values that originates is ($\tilde{\alpha} = 1.38, \tilde{Gr}_m = 0, \tilde{Gr} = 491.78$), which closely agree with those critical values mentioned in Belyaev and Smorodin [20]. I have computed the critical values for onset of the magnetic convection ($\tilde{Gr} = 0$) considering $\tilde{\chi} = \tilde{\chi}_* = 4$ and $\tilde{Pr} = 130$. The resulting critical values are $\tilde{\alpha} = 1.928$, and $\tilde{Gr}_m = 1.387$, which exhibit good agreement with the values of $\tilde{\alpha} = 1.95$ and $\tilde{Gr}_m = 1.385$ reported in Finlayson [11]. Furthermore, for mixed convection: the critical values are also computed for $\tilde{\chi} = \tilde{\chi}_* = 5$ and $\tilde{Pr} = 130$. Two sets of results are obtained: ($\tilde{\alpha} = 1.696, \tilde{Gr}_m = 15.775, \tilde{Gr} = 16.69$) as well as ($\tilde{\alpha} = 1.256, \tilde{Gr}_m = 1.40, \tilde{Gr} = 39.976$). These critical values demonstrate close agreement with the set of values reported in Suslov [15].

Flow Stability Diagrams for an Equivalent II-D Problem

The purpose of this section is to find parametric areas where various physical characteristics lead the beginning of instability in the geometry under consideration. The entire stability diagrams for an equivalent two-dimensional problem are accomplished to do this. In particular, the physical nature of instabilities is clearly defined as in the limits of $\tilde{Gr}_m \rightarrow 0$ (the thermogravitational convection: Type-I instability in the form of counter propagating thermal waves); $\tilde{Gr} \rightarrow 0$ (the stationary magneto-convection: Type-II instability characterizes the stationary rolls), and both $\tilde{Gr}_m \neq 0$ and $\tilde{Gr} \neq 0$ (the mixed convection: Type-III instability characterizing its parametric boundary is not continuously connected to either the $\tilde{Gr}_m = 0$ or $\tilde{Gr} = 0$ regimes) (see the figure placed in the first row in Figure 3) The corresponding typical eigen-value curves are shown in Figure 2. The physical activities inside the layer regarding the eigen-value curves reported in Figure 2 to be discussed details in the next section 6.3. To facilitate the further discussion the stability diagrams computed for identical physical parameters but for various field orientations are collected in Figure 3. The field inclination angle persists to be crucial in determining the flexible stability bounds of the investigated flow. The stability diagrams shown in the left column in Figure 3 consists of more than one line each representing a dissimilar instability characterized by its proper wave number represented by the corresponding graph plotted in the middle column for every row in this figure. Each of the graphs drawn in the right column in this figure represents the corresponding wave speed for various field inclination angles. It is found the qualitative change in the shape of stability diagrams with the change of field inclination angles. It concludes that, the flow stability regimes become larger as well as the symmetry of wave speeds broken completely in the flow domain with the increase of field inclination angle (Figure 3).

According to the stability diagram for an inclined magnetic field ($\delta = 8.5^\circ, \gamma = 0^\circ$) in the third row of Figure 3 the flow stabilizes significantly as δ increases (the area

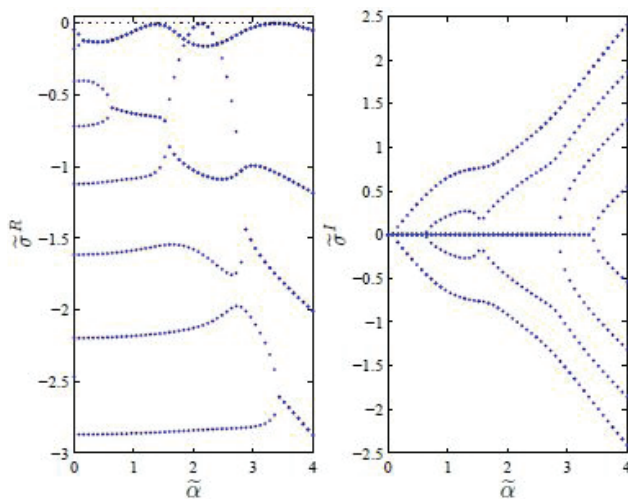


Figure 2. The leading disturbance speed amplification rate of $\tilde{\sigma}^R$ (on left) and the frequency of $\tilde{\sigma}^I$ (on right) are presented as functions of $\tilde{\alpha}$ for ($\tilde{Gr} = 11.75, \tilde{Gr}_m = 43.03$) at $\delta = 0^\circ = \gamma, \tilde{Pr} = 55$ and $\tilde{\chi} = \tilde{\chi}_* = 5$. The maxima on the left-and right existing in the left graph, correspond to the number of small and large waves, respectively, and the maximum on the middle corresponds with a static roll pattern.

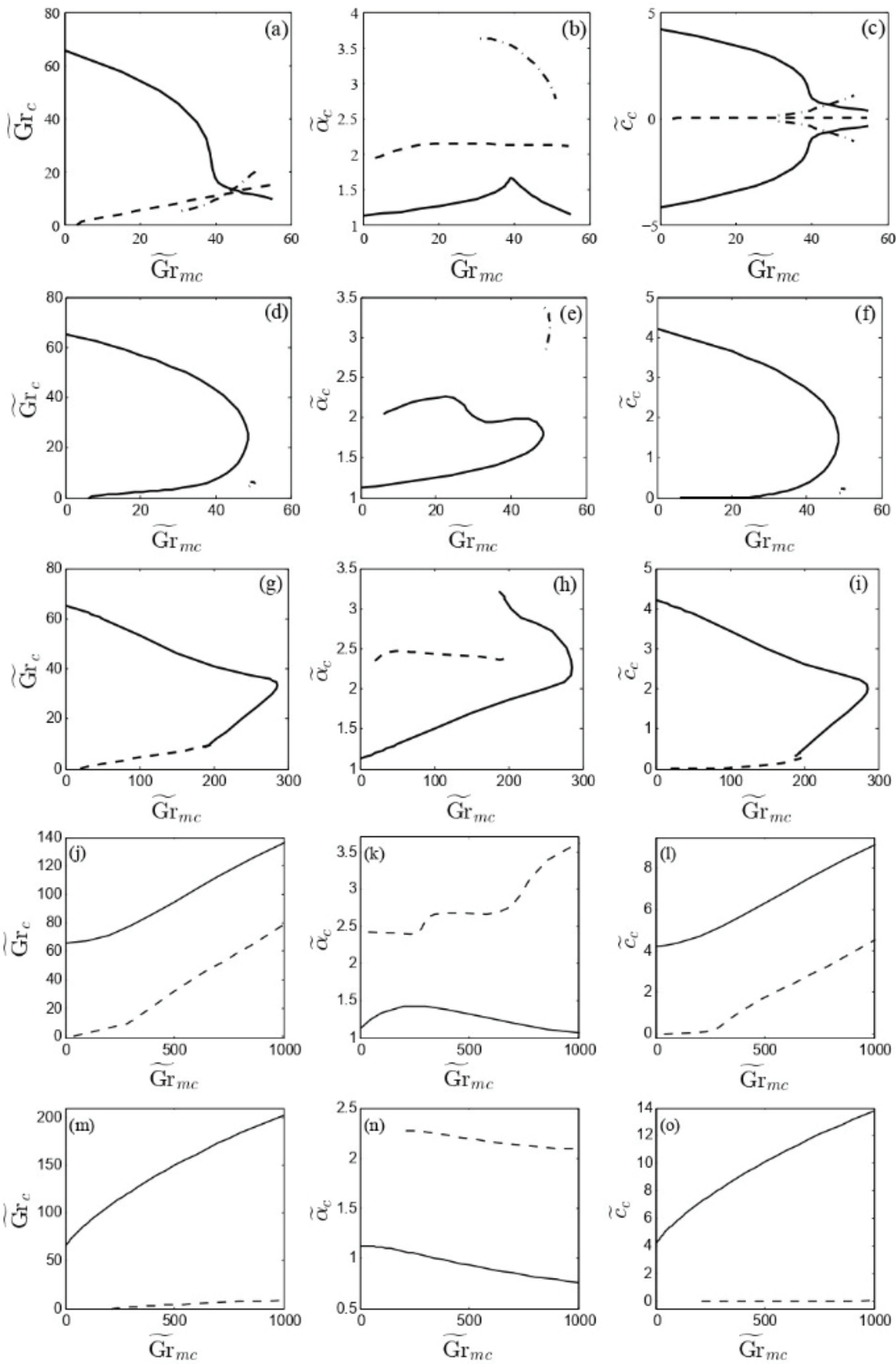


Figure 3. Variation of stability diagrams for $\widetilde{Pr} = 55$, $H^e = 100$, $\widetilde{\chi} = \widetilde{\chi}_* = 5$ in an inclined magnetic field with the values of $\gamma = 0^\circ$ and (top to bottom rows) $\delta = 0^\circ, 5^\circ, 8.5^\circ, 10^\circ$ and 15° .

enclosed by the dashed and solid lines). The Type-III instability disappears completely at the larger field inclination angles by merging with the Type-I instability, see the solid line curve in the wave number plot (h) in the third row in Figure 3 that now joins large and small wave number values. However, Type-I as well as Type-II instability are easily distinguished again even though the Type-II instability boundary now consistent with non-stationary pattern (see the dashed line in plot (i) in the third row in Figure 3). The waves propagate upward with magnetic Grashof numbers greater than zero continue to be the most hazardous than the downward waves.

Perturbation Energy Balance and Perturbation Fields

Though, the physical nature of instabilities is clearly identified and discussed earlier but it is not clear adequately what the dominant physical mechanism is when both $\widetilde{Gr}_m \neq 0$ and $\widetilde{Gr} \neq 0$, whether the dominant roles of various mechanisms swap and if so at what exactly values of the governing parameters. In order to answer these and other remaining questions the perturbation kinetic energy balance equations to be derived and the corresponding energy balance for linearized disturbances to be considered here. It is instructive to use the same method for estimating the energy balance to validate the physical characteristics of the produced instabilities that used for example in [16, 25, 29]. The momentum equations (21) and (22) are multiplied by the complex conjugate counter parts \tilde{u} and \tilde{v} respectively. The two equations are then added, and their sum is integrated across the fluid layer width to provide the following results:

$$\tilde{\sigma} \Sigma_k = \Sigma_{uv} + \Sigma_{Gr} + \Sigma_{vis} + \Sigma_{m1} + \Sigma_{m2}, \tag{28}$$

where

$$\Sigma_k = \int_{-1}^1 \underbrace{(|\tilde{u}|^2 + |\tilde{v}|^2)}_{E_k} d\tilde{x} > 0, \tag{29}$$

$$\Sigma_{vis} = \int_{-1}^1 \underbrace{-\left(\tilde{\alpha}^2(|\tilde{u}|^2 + |\tilde{v}|^2) + |D\tilde{u}|^2 + |D\tilde{v}|^2\right)}_{E_{vis}} d\tilde{x} = -1 \tag{30}$$

$$\Sigma_{uv} = \int_{-1}^1 \underbrace{-\left(D\tilde{v}_0\tilde{u}\bar{\tilde{v}} + i\tilde{\alpha}\tilde{v}_0(|\tilde{u}|^2 + |\tilde{v}|^2)\right)}_{E_{uv}} d\tilde{x}, \tag{31}$$

$$\Sigma_{Gr} = \int_{-1}^1 \underbrace{\widetilde{Gr}\tilde{\theta}\bar{\tilde{v}}}_{E_{Gr}} d\tilde{x}, \tag{32}$$

$$\Sigma_{m1} = \int_{-1}^1 \underbrace{-\widetilde{Gr}_m D\tilde{H}_{x0}\tilde{e}_{10}\bar{\tilde{\theta}}\tilde{u}}_{E_{m1}} d\tilde{x} \tag{33}$$

$$\Sigma_{m2} = \int_{-1}^1 E_{m2} d\tilde{x} \tag{34}$$

and

$$E_{m2} = -\widetilde{Gr}_m D\tilde{H}_{x0}\tilde{u}\frac{\partial\tilde{\theta}}{\partial\tilde{x}_0} \left((1 - \tilde{e}_{10}^2)D\tilde{\Phi} - i\tilde{\alpha}\tilde{e}_{10}\tilde{e}_{20}\tilde{\Phi} \right) - \widetilde{Gr}_m\tilde{\theta}_0(\tilde{e}_{10}\tilde{u}D^2\tilde{\Phi} + i\tilde{\alpha}(\tilde{e}_{10}\tilde{v} + \tilde{e}_{20}\tilde{u})D\tilde{\Phi} - \tilde{\alpha}^2\tilde{e}_{20}\tilde{v}\tilde{\Phi}).$$

The terms defined by (29)-(34) unambiguously represent the perturbation kinetic energy, the viscous dissipation, the energy interchange with the basic velocity field, the buoyancy, the variation of the fluid magnetization with the temperature and the variation of a magnetic field induced by the motion of ferrofluid, respectively. Equation (28) is just an integrated form of the linearized perturbation momentum equations (21) and (22) and thus it does not contain any new information on instabilities. However, it presents a straightforward and easy interpretation form at the crucial points $\tilde{\sigma}^R \equiv 0$. Thus, the real component in the right part of the equation (28) calculated at $(\widetilde{Gr}_c, \widetilde{Gr}_{mc})$ must be zero as well, and the positive terms in the right part of the equation (28) unambiguously indicate that the corresponding physical mechanism plays a destabilizing role and vice versa. The magnitude of each of the terms is an easy-to-read measure of the relative importance of the corresponding physical mechanism.

Note that the viscous dissipation term (30) is negatively defined and since the eigen-functions of the linearized problem are specified up to an arbitrary multiplicative constant, for convenience, the perturbation energy balance terms are normalized so that $\Sigma_{vis} \equiv -1$. Table 1 contains the numerical data for the perturbation energy integrals for various values of \tilde{X} and \tilde{X}^* at the critical points for the Type-I instability at $\widetilde{Gr}_m = 12$ in a normal field. The data in the table enables one to make a number of basic inferences regarding the driving mechanisms of the Type-I instability that are independent of whether the fluid is strongly or weakly magnetizable and of whether its magnetization law is linear or not. It is evident from Table 1 that the dominant physical mechanism leading to this type of instability is the gravitational buoyancy caused by the thermal disturbances because $Re(\Sigma_{Gr}) > 0$ and the magnitude of this term is much larger than that of any other energy terms (apart from the viscous dissipation term whose magnitude is set to 1). Thus, even when the $\widetilde{Gr}_m \neq 0$ the Type-I instability is similar to that caused by thermal waves observed in large-Prandtl-number nonmagnetic fluid. The dependence of the ferrofluids magnetization on the temperature also plays a destabilizing role ($Re(\Sigma_{m1}) > 0$). Therefore, in general the Type-I instability is caused by thermal perturbations that affect the fluid’s density and magnetization so that both Archimedean and Kelvin forces act together to destabilize the parallel basic flow. However, both $Re(\Sigma_{m2})$ and $Re(\Sigma_{uv})$ remain negative.

Therefore, the perturbation kinetic energy is lost not only due to the viscous dissipation, but also because it is

Table 1. Values of the perturbation energy integrals $\Sigma_k, \Sigma_{m1}, \Sigma_{m2}, \Sigma_{Gr}$ and Σ_{uv} computed for the Type-I instability in perpendicular magnetic field ($\delta = 0^\circ$) at $\widetilde{Gr}_m = 12, Pr = 55, H^e = 100$ and numerous values of $\tilde{\chi}$ and $\tilde{\chi}_*$ and at the corresponding critical values of $\tilde{\alpha}, \widetilde{Gr}$ given in Table 2 for the upward (odd lines) and downward (even lines) propagating waves.

$\tilde{\chi}$	$\tilde{\chi}_*$	Σ_k	$R(\Sigma_{m1})$	$I(\Sigma_{m1})$	$R(\Sigma_{m2})$	$I(\Sigma_{m2})$	$R(\Sigma_{Gr})$	$I(\Sigma_{Gr})$	$R(\Sigma_{uv})$	$I(\Sigma_{uv})$
5	5	0.0958	0.036	0.132	-0.017	-0.072	0.995	-0.468	-0.0141	-0.0261
		0.0958	0.036	-0.132	-0.017	0.072	0.995	0.468	-0.0141	0.0261
3	5	0.0955	0.036	0.131	-0.011	-0.062	0.992	-0.480	-0.0170	-0.0263
		0.0955	0.035	-0.129	-0.012	0.064	0.995	0.479	-0.0172	0.0267
3	3	0.0958	0.036	0.133	-0.016	-0.069	0.994	-0.469	-0.0142	-0.0259
		0.0958	0.036	-0.133	-0.016	0.069	0.994	0.469	-0.0142	0.0259
1.5	2.5	0.0957	0.037	0.135	-0.011	-0.058	0.989	-0.479	-0.0160	-0.0254
		0.0956	0.036	-0.133	-0.012	0.060	0.991	0.478	-0.0162	0.0258

Table 2. The critical values of $\tilde{\alpha}, \widetilde{Gr}$ and \tilde{c} for leading two waves of mixed convection for $H^e = 100, \widetilde{Gr}_m = 12, Pr = 55$ and various values of $\tilde{\chi}$ and $\tilde{\chi}_*$ in a normal magnetic field ($\delta = 0^\circ$)

Upward propagating wave					Downward propagating wave		
$\tilde{\chi}$	$\tilde{\chi}_*$	$\tilde{\alpha}$	\widetilde{Gr}	\tilde{c}	$\tilde{\alpha}$	\widetilde{Gr}	\tilde{c}
5	5	1.196	59.28	3.785	1.196	59.28	-3.785
3	5	1.204	59.52	3.795	1.199	60.27	-3.845
3	3	1.198	58.86	3.758	1.198	58.86	-3.758
1.5	2.5	1.207	58.18	3.708	1.202	58.84	-3.752
1	2	1.207	58.32	3.716	1.200	59.38	-3.786
0.5	1.5	1.202	59.50	3.790	1.193	61.53	-3.923

used to modify the applied magnetic field (field induction by moving ferrofluid) and to feed back to the parallel base velocity field, even though these two negative energy fluxes remain relatively weak. It also follows from Table 1 that the Type-I instability waves propagating upward and downward in a normal field are identical from the energy flux point of view. However closer to magnetic saturation when $\tilde{\chi} < \tilde{\chi}_*$ the upward propagating wave is characterized by a somewhat larger values of $Re(\Sigma_{m1})$ and smaller values of $Re(\Sigma_{Gr})$. This is consistent with the general observation made in the previous section that waves propagating upward become more dangerous when the relative magnetic effects rise. The imaginary parts of the energy integrals define the sign of $\tilde{\sigma}^l$ and thus of the spreading wave speed $\tilde{c} = \tilde{\sigma}^l / \tilde{\alpha}$. The corresponding data presented in Table 1 shows that $Im(\Sigma_{Gr})$ has the largest magnitude and therefore its sign defines the sign of \tilde{c} . Physically, this means that the motion of the Type-I instability patterns is mostly due to the gravitational buoyancy effects with a relatively weak contribution from the magnetic field ($Im(\Sigma_{m2})$) and the basic velocity field ($Im(\Sigma_{uv})$) effects. At the same time the variation of the fluid magnetization ($Im(\Sigma_{m1})$) hinders this motion. The disturbance energy data presented in

Table 3 for the Type-I instability waves in an oblique field reveals similar general trends, however, with one remarkable qualitative change: the $Re(\Sigma_{m2})$ values become positive. This indicates that in an oblique field the coupling between magnetic and velocity fields may have a destabilizing effect. The possible physical interpretation of this fact is that the inclined magnetic field drives the emerging convection flow patterns to re-orient aligning with the applied field's in-layer components.

While the data in Tables 1 and 3 demonstrates that for comparatively small values of \widetilde{Gr}_m the Type-I instability is mostly due to the gravitational buoyancy it is intuitively clear that magnetic effects must become progressively more important as the value of \widetilde{Gr}_m increases. This is indeed confirmed by Figure 4. In a normal field a sharp transition from the predominantly buoyancy to predominantly magnetically driven Type-I instability occurs when the ratio $\widetilde{Gr}_m / \widetilde{Gr}$ approaches a certain value (e.g. $\widetilde{Gr}_m / \widetilde{Gr} \sim 0.6$ for the fluid with properties chosen in Figure 4(a), see also [15] for the similar result for a ferrofluid with different properties). In fact, the gravitational buoyancy not only becomes less important, but it even starts to play a modestly stabilizing acts for large values of \widetilde{Gr}_m (dash-dotted line crosses

Table 3. Same as Table 1 but for an inclined magnetic field for ($\delta = 5^\circ, \gamma = 0^\circ$) and the critical values of $\tilde{\alpha}$ and \tilde{Gr} given in Table 4

$\tilde{\chi}$	$\tilde{\chi}_*$	Σ_k	$R(\Sigma_{m1})$	$I(\Sigma_{m1})$	$R(\Sigma_{m2})$	$I(\Sigma_{m2})$	$R(\Sigma_{Gr})$	$I(\Sigma_{Gr})$	$R(\Sigma_{uv})$	$I(\Sigma_{uv})$
5	5	0.0960	0.025	0.100	0.012	-0.090	0.975	-0.430	-0.0118	-0.0269
		0.0960	0.025	-0.099	0.011	0.089	0.976	0.430	-0.0118	0.0270
3	5	0.0959	0.022	0.087	0.027	-0.097	0.965	-0.420	-0.0131	-0.0278
		0.0961	0.021	-0.086	0.032	0.100	0.960	0.416	-0.0134	0.0275
3	3	0.0960	0.031	0.117	0.007	-0.083	0.975	-0.445	-0.0130	-0.0259
		0.0960	0.030	-0.117	0.007	0.083	0.975	0.445	-0.0130	0.0259
1.5	2.5	0.0959	0.031	0.118	0.017	-0.078	0.966	-0.449	-0.0145	-0.0254
		0.0959	0.030	-0.117	0.018	0.080	0.967	0.447	-0.0147	0.0256

Table 4. Same as Table 2 but for an inclined magnetic field for ($\delta = 5^\circ, \gamma = 0^\circ$)

$\tilde{\chi}$	$\tilde{\chi}_*$	Upward propagating wave			Downward propagating wave		
		$\tilde{\alpha}$	\tilde{Gr}	\tilde{c}	$\tilde{\alpha}$	\tilde{Gr}	\tilde{c}
5	5	1.196	60.69	3.893	1.194	60.86	-3.904
3	5	1.196	62.15	3.992	1.194	61.97	-3.985
3	3	1.207	58.91	3.770	1.206	58.99	-3.775
1.5	2.5	1.217	58.22	3.723	1.212	58.62	-3.751
1	2	1.220	57.93	3.702	1.214	58.54	-3.744
0.5	1.5	1.220	58.37	3.729	1.213	59.51	-3.808

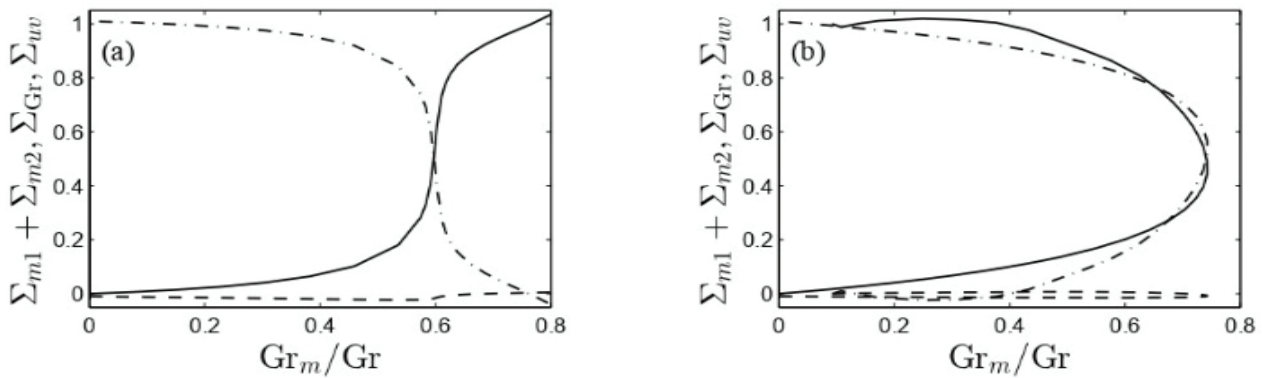


Figure 4. The perturbation energy integrals entering equation (6.1) characterizing the thermomagnetic ($\Sigma_{m1} + \Sigma_{m2}$, the solid line) and thermogravitational (Σ_{Gr} , the dash-dotted line) processes responsible for convection and the interchange with the basic flow (Σ_{uv} , the dashed line) as functions of the relation \tilde{Gr}_m/\tilde{Gr} along the stability boundaries drawn by solid lines (a) in Figure 3(a) placed in the 1st row for normal field, and (b) in Figure 3(d) placed in the 2nd row for oblique field.

the zero level in Figure 4(a) demonstrating that $\text{Re}(\Sigma_{Gr})$ becomes negative). At the same time the overall magnetic contribution to the perturbation energy is always non-negative. As a result, magnetic impacts are always destabilizing. The interaction of perturbations with the basic flow velocity field also starts playing a slightly destabilizing role for large \tilde{Gr}_m but this instability mechanism remains very

weak. Therefore, we conclude that the basic flow has little to do with the Type-I instability in a complete parametric range.

The similar energy diagram presented in Figure 4(b) constructed for an oblique magnetic field looks different because of the different pattern of the stability boundary depicted in Figure 3(a) placed in the 2nd row for an oblique

field. Note that if the solid curve in Figure 3(a) placed in the 2nd row is followed in the clockwise direction, then so is dash-dotted line in Figure 4(b), while the solid line in Figure 4(b) needs to be traced anti-clockwise. The two

curves intersect at $\widetilde{Gr}_m/\widetilde{Gr} \sim 0.75$. Therefore, the magnetic effects causing the Type-I instability overcome the gravitational buoyancy at much larger values of \widetilde{Gr}_m when the magnetic field is applied obliquely. This explains the

Table 5. Selected critical values of parameters and perturbation energy integrals (real parts) for $H^e = 100$, $\widetilde{Pr} = 55$ and $\tilde{\chi} = \tilde{\chi}_* = 5$

#	δ°	$\tilde{\gamma}^\circ$	$\tilde{\alpha}$	\widetilde{Gr}	\widetilde{Gr}_m	\tilde{c}	Σ_k	$R(\Sigma_{m1})$	$R(\Sigma_{m2})$	$R(\Sigma_{Gr})$	$R(\Sigma_{uv})$
1	0	0	1.383	11.75	43.03	0.540	0.0921	1.6782	-0.7230	0.0428	0.0014
2	0	0	2.125	11.75	43.03	0.000	0.0851	1.7815	-0.5826	-0.2063	0.0073
3	0	0	3.392	11.75	43.03	0.556	0.0557	1.5268	-0.3540	-0.1632	-0.0096
4	5	0	1.197	60.70	12.00	3.893	0.0960	0.0254	0.0116	0.9748	-0.0118
5	5	60	1.193	60.05	12.00	3.844	0.0959	0.0266	0.0011	0.9851	-0.0127
6	5	180	1.130	65.48	12.00	4.198	0.0956	0.0237	-0.0454	1.0334	-0.0117
7	10	0	1.156	65.55	12.00	4.225	0.0960	0.0129	0.0124	0.9835	-0.0088
8	10	75	1.165	62.30	12.00	3.997	0.0960	0.0149	0.0008	0.9960	-0.0116
9	10	180	1.088	70.53	12.00	4.541	0.0956	0.0122	-0.0485	1.0449	-0.0086
10	15	0	1.127	68.74	12.00	4.442	0.0960	0.0069	0.0067	0.9935	-0.0071
11	15	81	1.149	68.59	12.00	4.084	0.0960	0.0084	0.0001	1.0024	-0.0109
12	15	180	1.072	72.87	12.00	4.703	0.0956	0.0066	-0.0444	1.0445	-0.0068
13	8.5	0	2.369	8.90	187.30	0.215	0.0445	0.3285	0.5843	0.0827	0.0046
14	8.5	0	3.099	10.35	197.00	0.453	0.0459	0.4184	0.5024	0.0753	0.0039
15	10	0	2.401	7.00	232.31	0.098	0.0393	0.3586	0.5865	0.0525	0.0025
16	10	0	2.656	15.00	342.91	0.718	0.0490	0.2111	0.7121	0.0723	0.0045
17	10	0	3.394	65.00	860.54	3.680	0.0422	0.2295	0.6609	0.1420	-0.0325
18	5	52.5	1.802	7.17	35.00	0.306	0.0868	1.5429	-0.6071	0.0582	0.0060
19	5	125	2.110	7.97	35.00	0.002	0.0907	1.8653	-0.5095	-0.3533	-0.0026

Table 6. Selected critical values of parameters and perturbation energy integrals (imaginary parts) for $H^e = 100$, $\widetilde{Pr} = 55$ and $\tilde{\chi} = \tilde{\chi}_* = 5$

#	δ°	$\tilde{\gamma}^\circ$	$\tilde{\alpha}$	\widetilde{Gr}	\widetilde{Gr}_m	\tilde{c}	Σ_k	$R(\Sigma_{m1})$	$R(\Sigma_{m2})$	$R(\Sigma_{Gr})$	$R(\Sigma_{uv})$
1	0	0	1.383	11.75	43.03	0.540	0.0921	1.3698	-0.7731	-0.6700	0.0044
2	0	0	2.125	11.75	43.03	0.000	0.0851	0.0000	0.0000	0.0000	0.0000
3	0	0	3.392	11.75	43.03	0.556	0.0557	0.1760	-0.0909	-0.1672	-0.0230
4	5	0	1.197	60.70	12.00	3.893	0.0960	0.0994	-0.0898	-0.4300	-0.0269
5	5	60	1.193	60.05	12.00	3.844	0.0959	0.1012	-0.0680	-0.4466	-0.0265
6	5	180	1.130	65.48	12.00	4.198	0.0956	0.0914	-0.0598	-0.4557	-0.0296
7	10	0	1.156	65.55	12.00	4.225	0.0960	0.0541	-0.0919	-0.4015	-0.0297
8	10	75	1.165	62.30	12.00	3.997	0.0960	0.0581	-0.0399	-0.4373	-0.0277
9	10	180	1.088	70.53	12.00	4.541	0.0956	0.0498	-0.0609	-0.4293	-0.0322
10	15	0	1.127	68.74	12.00	4.442	0.0960	0.0301	-0.0892	-0.3900	-0.0314
11	15	81	1.149	68.59	12.00	4.084	0.0960	0.0334	-0.0226	-0.4327	-0.0284
12	15	180	1.072	72.87	12.00	4.703	0.0956	0.0281	-0.0637	-0.4132	-0.0333
13	8.5	0	2.369	8.90	187.30	0.215	0.0445	0.6776	-0.7004	-0.0069	0.0070
14	8.5	0	3.099	10.35	197.00	0.453	0.0459	1.0567	-1.1214	-0.0199	0.0202
15	10	0	2.401	7.00	232.31	0.098	0.0393	0.3726	-0.3876	0.0025	0.0033
16	10	0	2.656	15.00	342.91	0.718	0.0490	1.1415	-1.2589	-0.0027	0.0268
17	10	0	3.394	65.00	860.54	3.680	0.0422	0.7930	-1.3077	-0.0615	0.0485
18	5	52.5	1.802	7.17	35.00	0.306	0.0868	1.2272	-0.9240	-0.3555	0.0044
19	5	125	2.110	7.97	35.00	0.002	0.0907	-0.0074	0.0077	-0.0006	-0.0001

qualitative change in the shape of the instability boundary that is observed when the field inclination angle is increased and is demonstrated in Figure 3, compare the third and fourth rows there: starting from some field inclination angle $8.5^\circ < \delta < 10^\circ$ the Type-I instability remains dominated by the gravitational buoyancy regardless of the value of \widetilde{Gr}_m . This can be traced back to the geometric mitigation of the cross-layer x portion of the applied field that is mostly responsible for thermomagnetic contrivance of instability. The interaction of the Type-I instability fields with that of the primary flow velocity remains negligible. The consideration of disturbance energy integrals serves as a useful tool for clarifying and distinguishing between the physical mechanisms behind various instabilities.

The data for several parametric points of interest is collected in Tables 5 and 6. Rows 1-3 correspond to the three $\widetilde{\sigma}^R$ maxima in Figure 3 that distinguish the Types I, II and III instabilities. The comparison of real parts

of the integrals confirms that in normal field the destabilization of the basic flow is achieved primarily due to the thermal variation of fluid's magnetization $\text{Re}(\Sigma_{m1})$. The main feature that distinguishes the Type-I instability from its Type-III counterpart is that even though as \widetilde{Gr}_m increases the magnetic effects become dominant for both of them the gravitational buoyancy still remains a destabilizing factor for the Type-I instability while for the Type-III instabilities the driving mechanism is purely magnetic. As expected from the previous discussion this is also so for the Type-II instability. The energy exchange with the basic velocity field remains negligible for all three instability types. Thus, the presence of a specific cubic velocity profile is rather inconsequential in the considered problem. Note also that while the roles of the buoyancy (Σ_{Gr}) and the magnetic field variation (Σ_{m2}) in supporting the instabilities at the large values of \widetilde{Gr}_m are relatively weak the inspection of imaginary parts of the energy integrals

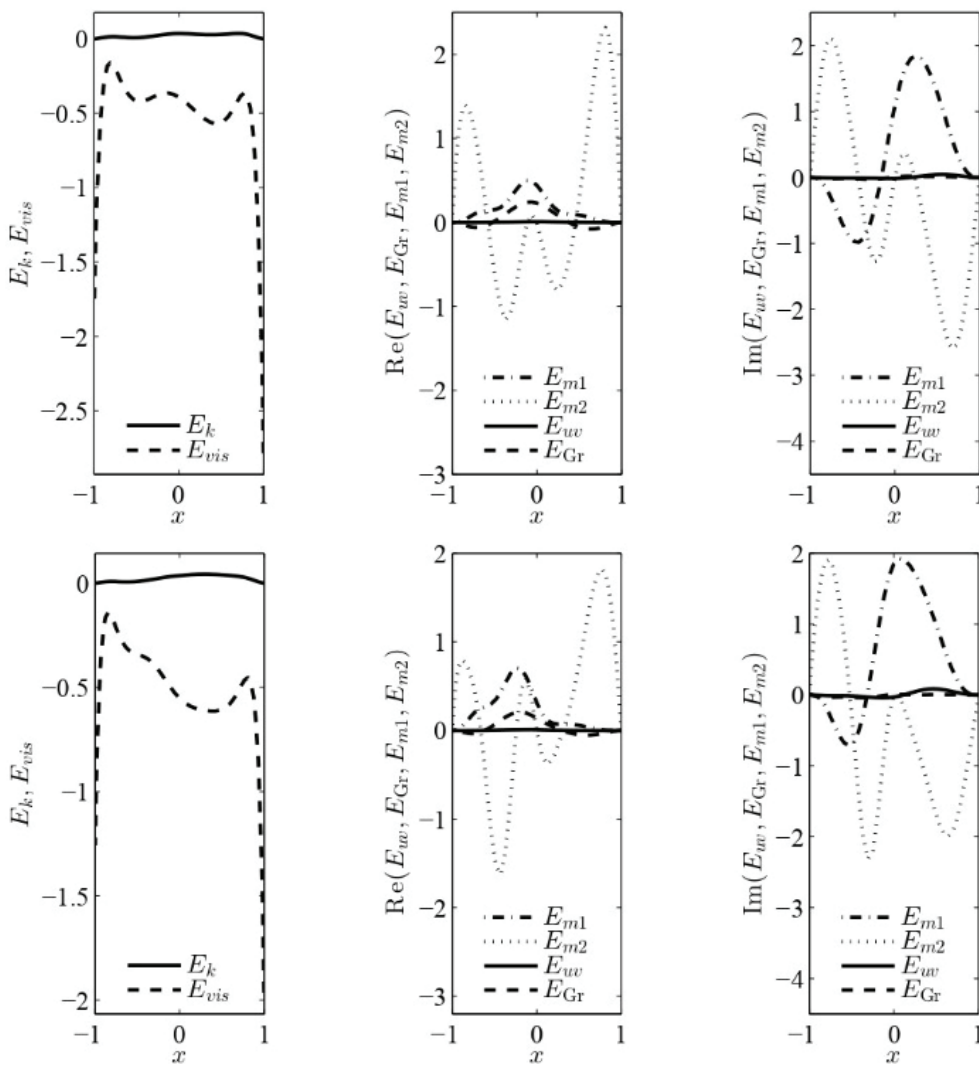


Figure 5. Disturbance energy integrands for $\delta = 8.5^\circ$, $\gamma = 0^\circ$, $\widetilde{Pr} = 55$, $H^e = 100$ and $\widetilde{\chi} = \widetilde{\chi}_* = 5$ at the critical points related to the parameters listed in rows 13 (top) and 14 (bottom) in Tables 5 and 6.

shows that the combination of these two influences defines the propagation direction of the disturbance wave for both Type-I and Type-III instabilities. Rows 4-12 in Tables 5 and 6 characterize the Type-I instability observed for various field orientations. In this case the ratio of $\widetilde{Gr}_m/\widetilde{Gr}$ does not exceed 0.2 and consistent with Figure 4 the instability is mostly driven by the gravitational buoyancy with a relatively small contribution from magnetic effects. However, the data in Tables 5 and 6 suggest a remarkable conjecture. The optimal orientation γ_{min} of the magnetic field when the Type-I instability is promoted the most corresponds to the regime for which $Re(\Sigma_{m2})$ vanishes that

is to the situation when the secondary flow arising due to the developing disturbances does not lead to the integral variation of the applied magnetic field. Rows 13 and 14 in Tables 5 and 6 illustrate a switch between the two instability patterns with significantly different wavenumbers that occur when the field inclination angle becomes sufficiently large as seen in the third row in Figure 3. The data presented in the table indicate that neither buoyancy nor the basic flow velocity field are responsible for such a transition. The physical distribution of the energy integrands presented in Figure 5 also confirms that (see the solid and dashed lines in the middle panels).

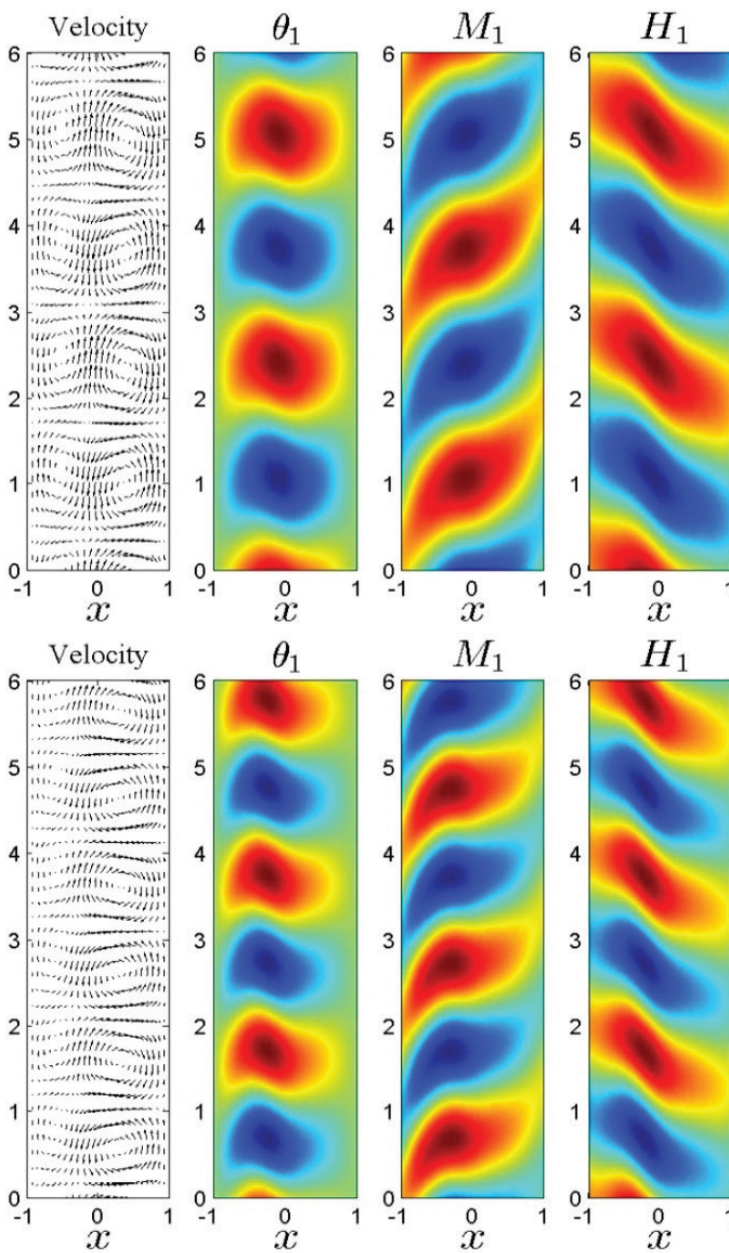


Figure 6. Disturbance fields for $\delta = 8.5^\circ$, $\gamma = 0^\circ$, $\widetilde{Pr} = 55$, $He = 100$ and $\tilde{\chi} = \tilde{\chi}_* = 5$ at the critical points related to the parameters listed in rows 13 (top) and 14 (bottom) in Tables 5 and 6. Cross-section along the main periodicity direction.

Qualitatively, the disturbance energy distributions for both patterns remain similar, which allows one to conclude that physical mechanism of instability is the same for both type of patterns. As seen from middle panels in Figure 5 the destabilizing magnetic field variation effect (Σ_{m2}) is most pronounced in the near-wall regions, especially near the right cold wall (dotted line in the middle panels). However, the viscous dissipation there is also stronger than that adjacent the hot wall (dashed line in the left panels). As a result, the overall instability pattern shifts toward the hot wall as seen in the bottom row of Figure 6. The main observable features distinguishing the two switching patterns are their wave numbers (compare perturbation patterns shown in Figure 6) and propagation speeds: both increase discontinuously at the transition point. Such an increase is fully due to magnetic effects, compare the corresponding entries for ($\text{Im}(\Sigma_{m1})$ and $\text{Im}(\Sigma_{m2})$) in rows 13 and 14 of the Tables 5 and 6. The data in rows 15–17 in Tables 5 and 6 that refer to the fourth row of plots in Figure 3 indicate that similar magnetically influenced transitions occur at larger values of the field inclination angle as the magnetic Grashof number

increases. Even though the pattern wavenumber changes in a stepwise manner the transitions now are continuous. The data presented in rows 13–17 provides additional insights into the relationship between field orientation and the destabilization mechanisms. As the field inclination angle increases, a notable trend emerges: the dominant destabilization mechanism shifts from the thermomagnetic destabilization caused by the diversity of fluid magnetization with temperature $\text{Re}(\Sigma_{m1})$ to the destabilization brought on by the combined effects of the perturbed velocity field with induced variations in the magnetic field $\text{Re}(\Sigma_{m2})$. This shift indicates that, the data analysis reveals that with an increase in the field inclination angle, and thus the significance of thermomagnetic destabilization decreases, while the destabilization due to the interaction of the perturbed velocity field with induced magnetic field variations becomes more prominent. This emphasizes the importance of considering the interplay between fluid dynamics and magnetic field effects in understanding the overall stability behavior of the system. This is also confirmed by the energy integrand plots in the middle panels in Figure 7.

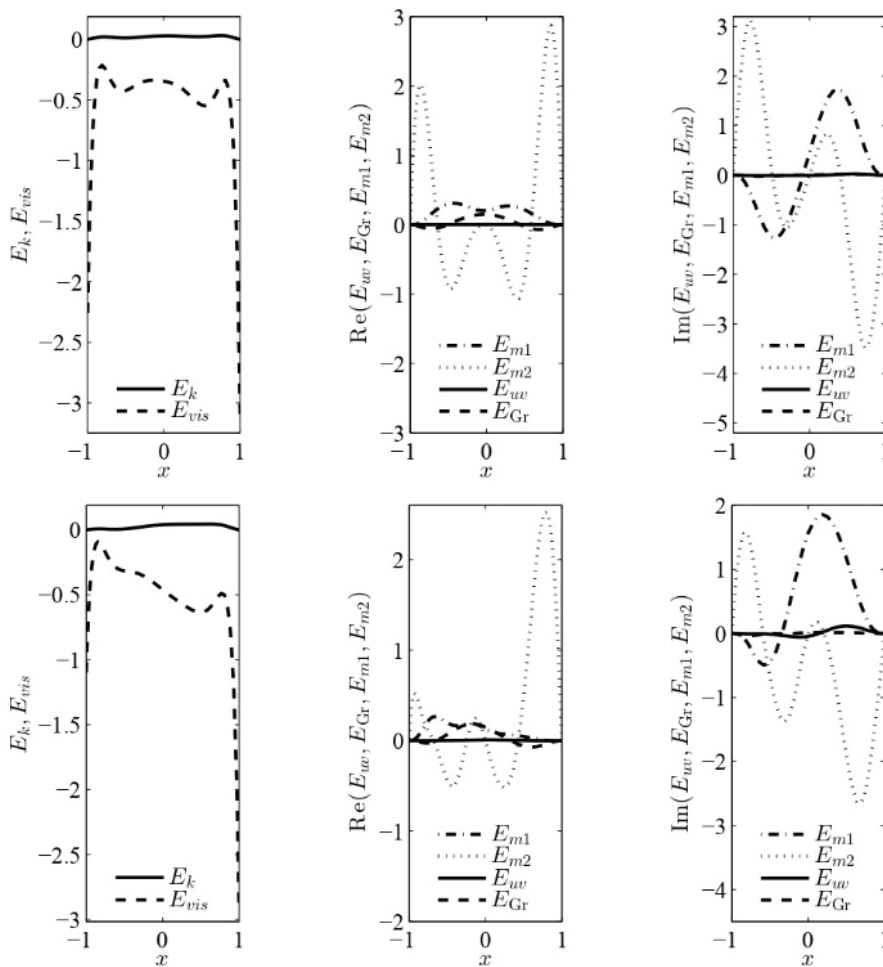


Figure 7. Disturbance energy integrands for $\delta = 10^\circ$, $\gamma = 0^\circ$, $\overline{\text{Pr}} = 55$, $H^e = 100$ and $\tilde{\chi} = \tilde{\chi}_* = 5$ at the critical points related to the parameters listed in rows 15 (top) and 16 (bottom) in Tables 5 and 6.

As the value of \widetilde{Gr}_m increases the maximum of the disturbance energy production $Re(\Sigma_{m2})$ (dotted line) shifts toward the cold wall where the basic flow magnetic field is weaker and its relative height increases. At the same time the maximum of the disturbance energy production $Re(\Sigma_{m1})$ (dash-dotted line) shifts to the hot wall where the basic flow fluid magnetization is weaker. Thus, the thermo-magnetic perturbations arising in the layer of ferrofluid tend to make the magnetic and magnetization fields there more uniform. Following a hydrodynamic analogy when perturbations lead to mixing the fluid making its velocity and temperature fields more uniform here one can introduce the concept of thermomagnetic mixing

when magnetically driven perturbations tend to make magnetic and magnetization fields more uniform. This is also illustrated in disturbance field plots in Figure 8, where the shift of the perturbation fields is seen to occur as \widetilde{Gr}_m increases, which is followed by the decrease of the disturbance wavelength. A further increase of \widetilde{Gr}_m leads to yet another qualitative change. As is evidenced by Figures 9 and 10 the cross-layer symmetry of the perturbation fields is lost completely with all perturbations shifted closer to the hot wall. Such a cross-layer localization (that is consistent with the previously made conclusion that the thermo-magnetic instability waves are most dangerous near the hot wall) is followed by the corresponding

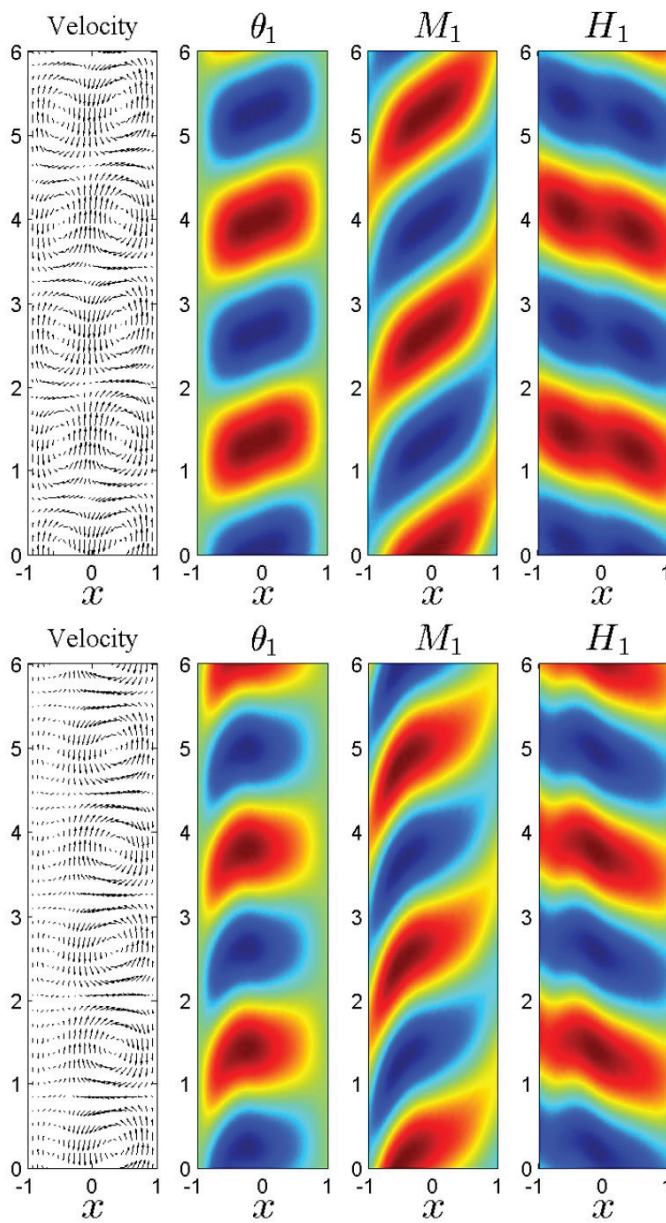


Figure 8. Disturbance fields for $\delta = 10^\circ$, $\gamma = 0^\circ$, $\overline{Pr} = 55$, $H^e = 100$ and $\tilde{\chi} = \tilde{\chi}_* = 5$ at the critical points related to the parameters listed in rows 15 (top) and 16 (bottom) in Tables 5 and 6. Cross-section along the main periodicity direction.

decrease of the disturbance wavelength or, equivalently, by the increase in the disturbance wave number, which is seen in the $\tilde{\alpha}$ plot in the fourth row in Figure 3. Lastly, the chosen parameter values like; ($\tilde{\gamma} = 52.5^\circ$, $\overline{Gr} = 7.168$), and ($\tilde{\gamma} = 125^\circ$, $\overline{Gr} = 7.971$) provided in rows 18 and 19, respectively in Tables 5 and 6 indicate that in an inclined field at comparatively large values of the magnetic Grashof

number either the Type-I or Type-II instability can arise and dominate the flow depending on the field azimuthal angle $\tilde{\gamma}$. The row 18 corresponds to the Type-I instability because both magnetic as well as gravitational buoyancy effects are destabilizing, while the row 19 illustrates the Type-II instability which is fully magnetically driven with buoyancy playing a stabilizing role.

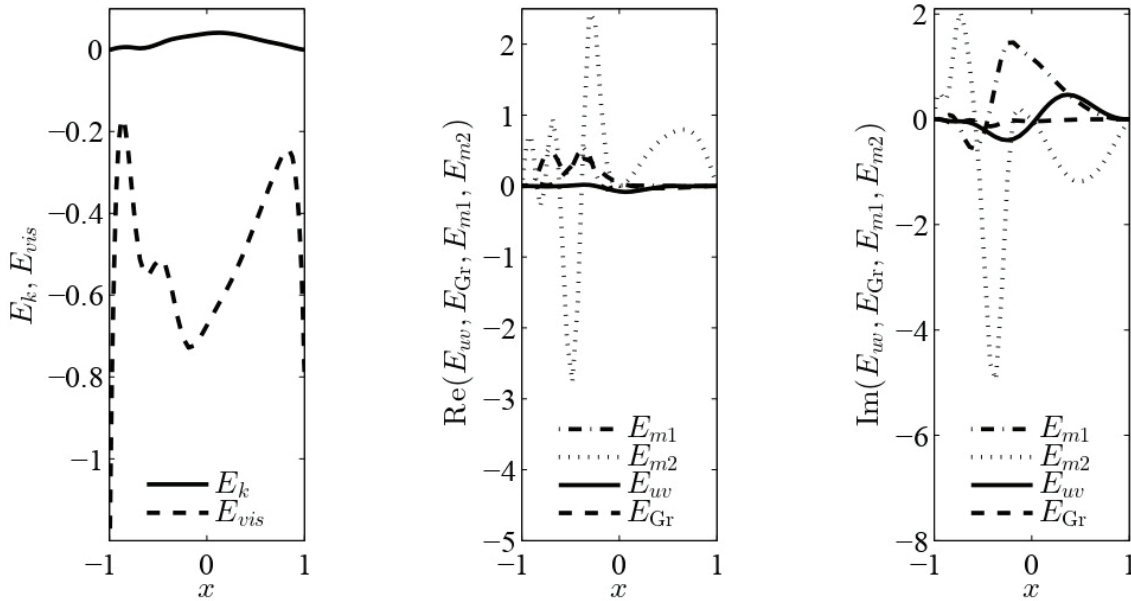


Figure 9. Disturbance energy integrands for $\delta = 10^\circ$, $\gamma = 0^\circ$, $\overline{Pr} = 55$, $H^e = 100$ and $\tilde{\chi} = \tilde{\chi}_* = 5$ at the critical points related to the parameters listed in row 17 in Tables 5 and 6.

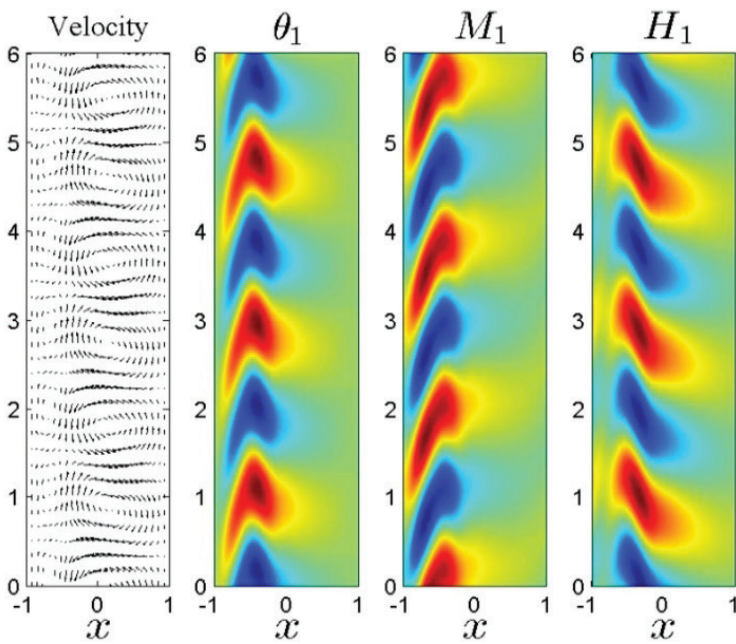


Figure 10. Disturbance fields for $\delta = 10^\circ$, $\gamma = 0^\circ$, $\overline{Pr} = 55$, $H^e = 100$ and $\tilde{\chi} = \tilde{\chi}_* = 5$ at the critical points related to the parameters listed in row 17 in Tables 5 and 6. Cross-section along the main periodicity direction.

CONCLUSION

The linear stability and energy distribution of thermo-magnetic gravitational convective flow in a vertical layer are investigated. At various values of the governing physical parameters, the instability modes are analyzed as functions of the intensity of magnetic field as well as the field orientation and inclination angles. A preferred field orientation angle coexists for every inclination angle that maximizes the onset of magnetogravitational instability. However, in the case of pure thermomagnetic instability, it is found that the most favorable configuration is the inclined magnetic field on the layer. On the other hand, the optimal field orientation for other types of instabilities is contingent upon the specific governing physical parameters. It is also found that the qualitative change in the instability patterns, and the area of flow stability become larger when the inclination angle increases. One significant finding is that the variation of fluid magnetization caused by thermal disturbances consistently leads to destabilization. This means that thermal disturbance always has an inherent destabilizing effect on the convective flow system. It is observed that two waves propagate inside the magnetogravitational instability regime; one of them goes up near the hot wall and the other goes down near the cold wall. However, the upward wave is more dangerous in all regimes compared to the downward one, regardless of whether the law of fluid magnetization is linear or not.

The interaction of perturbations with the basic flow velocity field is shown to remain weak in all regimes, so that the energy exchange between them is always insignificant for all three types of instability. In contrast, the role of gravitational buoyancy is always important, however. It is destabilizing when the thermal Grashof number is larger compared to the magnetic Grashof number, but it becomes stabilizing in magnetically dominated regimes. The thermomagnetic perturbations arising in the ferrofluid layer tend to prepare the magnetic and magnetization fields more uniform in regions dominated by magnetic field. The instability pattern shifts predominantly toward the hot wall of the fluid layer. The cross-layer symmetry of the perturbation fields is destroyed completely in the regimes near the hot wall. However, the thermomagnetic instability waves become most dangerous closer to the hot wall. This kind of convective flow characteristic is consistent with earlier studies and points to a novel physical mechanism for this investigation.

AUTHORSHIP CONTRIBUTIONS

Authors equally contributed to this work.

DATA AVAILABILITY STATEMENT

The authors confirm that the data that supports the findings of this study are available within the article. Raw data that support the finding of this study are available from the corresponding author, upon reasonable request.

CONFLICT OF INTEREST

The author declared no potential conflicts of interest with respect to the research, authorship, and/or publication of this article.

ETHICS

There are no ethical issues with the publication of this manuscript.

REFERENCES

- [1] Bashtovoy VG, Berkovsky BM, Vislovich AN. Introduction to thermomechanics of magnetic fluids. New York: Hemisphere Publishing; 1988.
- [2] Odenbach S. Microgravity experiments on thermomagnetic convection in magnetic fluids. *J Magn Magn Mater* 1995;149:155-157. [\[CrossRef\]](#)
- [3] Polevikov VK, Fertman VE. Investigation of heat transfer through a horizontal layer of a magnetic liquid for the cooling of cylindrical conductors with a current. *Magnetohydrodynamics* 1977;13:11-16.
- [4] Yamaguchi H, Zhang Z, Shuchi S, Shimada K. Heat transfer characteristics of magnetic fluid in a partitioned rectangular box. *J Magn Magn Mater* 2002;252:203-205. [\[CrossRef\]](#)
- [5] Charles SW. The Preparation of magnetic fluids. In: Odenbach S, editor. *Ferrofluids - Lecture Notes in Physics*. Berlin: Springer; 2002. pp. 3-18. [\[CrossRef\]](#)
- [6] Bozhko AA, Putin GF. Heat transfer and flow patterns in ferrofluid convection. *Magnetohydrodynamics* 2003;39:147-169. [\[CrossRef\]](#)
- [7] Zablotsky D, Mezulis A, Blums E. Surface cooling based on thermomagnetic convection: Numerical simulation and experiment. *Int J Heat Mass Transf* 2009;52:5302-5308. [\[CrossRef\]](#)
- [8] Mahfoud B, Moussaoui M. Buoyancy force and magnetic field effects on laminar vortex breakdown and fluid layers. *J Ther Engineer* 2023;9:12-23. [\[CrossRef\]](#)
- [9] Ghamati M, Askari N, Abbasi M, Moghimi SM, Khodadi SM, Taheri MH. Numerical analysis of coupled fluid flow and natural heat transfer on a vertical flat plate. *J Ther Engineer* 2024;10:1-9. [\[CrossRef\]](#)
- [10] Chandrasekhar S. *Hydrodynamic and hydromagnetic stability*. New York: Courier Corporation; 1981.
- [11] Finlayson BA. Convective instability of ferromagnetic fluids. *J Fluid Mech* 1970;40:753-767. [\[CrossRef\]](#)
- [12] Bozhko AA, Putin GF. Experimental investigation of thermo-magnetic convection in uniform external field. *Bull Acad Sci* 1991;55:1149-1156.
- [13] Shliomis MI, Smorodin BL. Convective instability of magnetized ferrofluids. *J Magn Magn Mater* 2002;252:197-202. [\[CrossRef\]](#)
- [14] Hennenberg M, Wessow B, Slavtchev S, Desai Th, Scheild B. Steady flows of laterally heated ferrofluid layer: Influence of inclined strong magnetic field and gravity level. *Phys Fluids* 2006;18:093602. [\[CrossRef\]](#)

- [15] Suslov SA. Thermomagnetic convection in a vertical layer of ferromagnetic fluid. *Phys Fluids* 2008;20:084101. [\[CrossRef\]](#)
- [16] Suslov SA, Bozhko AA, Sidorov AS, Putin GF. Thermomagnetic convective flows in a vertical layer of ferrocolloid: Perturbation energy analysis and experimental study. *Phys Rev E Stat Nonlin Soft Matter Phys* 2012;86:016301. [\[CrossRef\]](#)
- [17] El-Zahar ER, Rashad AM, Saddek LF. The impact of sinusoidal surface temperature on the natural convective flow of a ferrofluid along a vertical plate. *Mathematics* 2019;7:1014. [\[CrossRef\]](#)
- [18] Chamkha AJ, Rashad AM, Alsabery AI, Abdelrahman ZMA, Nabwey HA. Impact of partial slip on magneto-ferrofluids mixed convection flow in enclosure. *J Ther Sci Engineer Appl* 2020;12:051002. [\[CrossRef\]](#)
- [19] Taskesen E, Dirik M, Tekir M, Pazarlioglu HK. Predicting heat transfer performance of Fe₃O₄-cu/water hybrid nanofluid under constant magnetic field using ANN. *J Ther Engineer* 2023;9:811-822. [\[CrossRef\]](#)
- [20] Belyaev AV, Smorodin BL. The stability of ferrofluid flow in a vertical layer subject to lateral heating and horizontal magnetic field. *J Magn Magn Mater* 2010;322:2596-2606. [\[CrossRef\]](#)
- [21] Bozhko AA, Putin GF, Sidorov AS, Suslov SA. Convection in a vertical layer of stratified magnetic fluid. *Magneto hydrodynamics* 2013;49:143-152. [\[CrossRef\]](#)
- [22] Rahman H, Suslov SA. Thermomagnetic convection in a layer of ferrofluid placed in a uniform oblique external magnetic fluid. *J Fluid Mech* 2015;764:316-348. [\[CrossRef\]](#)
- [23] Rahman H, Suslov SA. Magneto-gravitational convection in a vertical layer of ferrofluid in a uniform oblique magnetic fluid. *J Fluid Mech* 2016;795:847-875. [\[CrossRef\]](#)
- [24] Rosensweig RE. *Ferrohydrodynamics*. Cambridge: Cambridge University Press; 1985.
- [25] Suslov SA, Bozhko AA, Putin GF. Thermomagneto-convective instabilities in a vertical layer of ferro-magnetic fluid. Available at: <https://citeseerx.ist.psu.edu/document?repid=rep1&type=pdf&doi=10a53ce56b2298ffee69c77e7379c44d2d91aebf>. Accessed Jun 26, 2024.
- [26] Ku HC, Hatzivramidis D. Chebyshev expansion methods for the solution of the extended Graetz problem. *J Comput Phys* 1984;56:495-512. [\[CrossRef\]](#)
- [27] Hatzivramidis D, Ku HC. An integral Chebyshev expansion method for boundary-value problems of ODE. type. *Comput Math Appl* 1985;11:581-586. [\[CrossRef\]](#)
- [28] Suslov SA, Paolucci S. Stability of mixed-convection flow in a tall vertical channel under non-Boussinesq conditions. *J Fluid Mech* 1995;302:91-115. [\[CrossRef\]](#)
- [29] Hart JE. Stability of the flow in a differentially heated inclined box. *J Fluid Mech* 1971;47:547-576. [\[CrossRef\]](#)